Accepted Manuscript

Carbon-assisted catalyst pretreatment enables straightforward synthesis of high-density carbon nanotube forests

Nicholas T. Dee, Jinjing Li, Alvin Orbaek White, Christine Jacob, Wenbo Shi, Piran R. Kidambi, Kehang Cui, Dmitri N. Zakharov, Nina Z. Janković, Mostafa Bedewy, Cécile A.C. Chazot, Jennifer Carpena-Núñez, Benji Maruyama, Eric A. Stach, Desiree L. Plata, A. John Hart
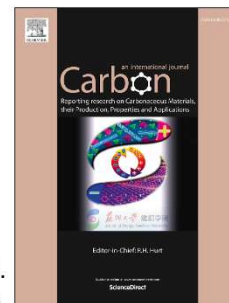
Please cite this article as: N.T. Dee, J. Li, A.O. White, C. Jacob, W. Shi, P.R. Kidambi, K. Cui, D.N. Zakharov, N.Z. Janković, M. Bedewy, Cé.A.C. Chazot, J. Carpena-Núñez, B. Maruyama, E.A. Stach, D.L. Plata, A.J. Hart, Carbon-assisted catalyst pretreatment enables straightforward synthesis of high-density carbon nanotube forests, *Carbon* (2019), doi: https://doi.org/10.1016/j.carbon.2019.06.083.

This is a PDF file of an unedited manuscript that has been accepted for publication. As a service to our customers we are providing this early version of the manuscript. The manuscript will undergo copyediting, typesetting, and review of the resulting proof before it is published in its final form. Please note that during the production process errors may be discovered which could affect the content, and all legal disclaimers that apply to the journal pertain.
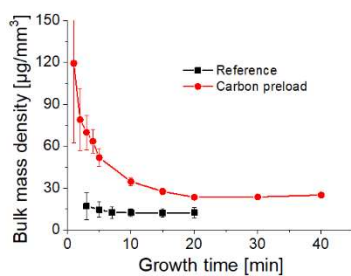
1　**Carbon-Assisted Catalyst Pretreatment Enables Straightforward Synthesis of High-**
2　**Density Carbon Nanotube Forests**
3

4　Nicholas T. Dee,[1] Jinjing Li,[1] Alvin Orbaek White,[1,2] Christine Jacob,[1] Wenbo Shi,[3,4] Piran R.
5　Kidambi,[1,5] Kehang Cui,[1] Dmitri N. Zakharov,[6] Nina Z. Janković,[3,4] Mostafa Bedewy,[1,7] Cécile
6　A. C. Chazot,[8] Jennifer Carpena-Núñez,[6,9] Benji Maruyama,[9] Eric A. Stach,[6,10] Desiree L.
7　Plata,[3,4] and A. John Hart[1,*]
8
9　[1]Department of Mechanical Engineering, Massachusetts Institute of Technology, Cambridge, MA 02139,
10　　USA
11　[2]Energy Safety Research Institute, Swansea University, Bay Campus, Swansea SA1 8EN, United
12　　Kingdom
13　[3]Department of Chemical and Environmental Engineering, Yale University, New Haven CT 06511
14　[4]Department of Civil and Environmental Engineering, Massachusetts Institute of Technology, Cambridge,
15　　MA 02139, USA
16　[5]Department of Chemical and Biomolecular Engineering, Vanderbilt University, Nashville, TN 37212,
17　　USA
18　[6]Center for Functional Nanomaterials, Brookhaven National Laboratory, Upton, NY 11973, USA
19　[7]Department of Industrial Engineering and Department of Chemical and Petroleum Engineering,
20　　University of Pittsburgh, Pittsburgh, PA 15261, USA
21　[8]Department of Materials Science and Engineering, Massachusetts Institute of Technology, Cambridge,
22　　Massachusetts 02139, United States
23　[9]Materials and Manufacturing Directorate, Air Force Research Laboratory, Wright-Patterson Air Force
24　　Base, Dayton, OH 45431, USA
25　[10]Department of Materials Science and Engineering, University of Pennsylvania, Philadelphia, PA 19104,
26　　USA
27
28
29　**ABSTRACT**
30

31　Despite extensive academic and commercial development, a comprehensive understanding of the

32　principles necessary for high-yield production of carbon nanotubes (CNTs) is lacking, whether in

33　oriented films, bulk powders, or other forms. In chemical vapor deposition growth of CNT films

34　on substrates, trace contaminants of carbon, such as deposits on the reactor tube walls, are known

35　to cause inconsistency in key production metrics, including CNT density and alignment. In this

36　study, we show that trace exposure of the catalyst to carbon during initial heating of the catalyst

37　film is a critical determinant of CNT yield, and this carbon exposure accelerates catalyst

38　nanoparticle formation *via* film dewetting and increases the probability of CNT nucleation and

39　the resultant density of the CNT population. By controlled exposure of the catalyst to a trace

40　amount of carbon, we show up to a 4-fold increase in bulk mass density for a given forest height,

41　an 8-fold increase in local CNT number density, and a 2-fold increase in the growth lifetime,

43　　exposure on the probability of CNT nucleation from nanoparticle catalysts, supported by

44　　microscopy and gas analysis.

45   **1. Introduction**

46   High density vertically aligned carbon nanotubes (CNT "forests") are useful for many

47   applications including thermal interface materials [1,2], electronic via interconnects [3,4],

48   supercapacitor electrodes [5,6], and nanoporous membranes [7,8]. While chemical vapor

49   deposition (CVD) has emerged as a favorable route for CNT synthesis, a comprehensive

50   understanding of growth processes remains incomplete [9], particularly the complex

51   relationships between the catalyst and support materials [10–13] and the interactions between

52   catalyst and carbon species that contribute to CNT nucleation [14,15]. This is attributed partly to

53   the large CVD process parameter space – catalyst materials, carbon feedstock, pressure,

54   temperature, moisture levels, and other variables all impact CNT growth [16] – and the often

55   empirical nature of research in the field.

56   Many catalyst-substrate combinations have been used for CNT growth by CVD, perhaps

57   most commonly a thin film of Fe catalyst on an Al_2O_3 support layer on a Si/SiO_2 substrate. Upon

58   reduction, the Fe film dewets and forms nanoparticles from which CNTs can nucleate in the

59   presence of a hydrocarbon precursor.   However, the density of CNTs can be limited by:

60   incomplete or nonuniform dewetting of the deposited film [17,18], coarsening of the formed

61   catalyst nanoparticles [12,18], incomplete activation of the particles to nucleate CNTs [17,19],

62   and premature deactivation of particles [20–22], preventing long CNT growth. Nevertheless, the

63   Fe/Al_2O_3 system has been used to form vertically aligned CNT forests using a wide range of

64   CVD chemistries resulting in both single-walled and multi-walled CNTs under appropriate

65   conditions.

66   A further understanding of the factors influencing the formation of active nanoparticle

67   catalysts from the deposited Fe film, and their interaction with the support layer, is essential to

68   enable reliable and scalable growth of high-density CNT forests. The deposited Fe film readily

69   oxidizes upon exposure to air, and reduction of the resulting oxide film is necessary for

70   dewetting and subsequent CNT nucleation [17,23,24]. Using *in situ* X-ray diffraction, X-ray

71   reflectivity, and environmental transmission electron microscopy (ETEM), Wirth *et al.* reported

72   that the active phase of the Fe catalyst for CNT growth (with an Al_2O_3 support) is kinetically

73   controlled. When the initial catalyst particle distribution is dominated by the γ-Fe (FCC) phase,

74   CNTs grow from γ-Fe or α-Fe (BCC) particles; yet, when the catalyst particles are initially α-Fe,

76   was necessary for CNT growth, and that the catalytically inactive Fe_5C_2 phase can form under

77   CNT growth conditions [26]. Furthermore, Oshima *et al*. observed that without an Al_2O_3

78   support layer, α-Fe can be converted into Fe_2SiO_4 while heating, and both phases are carbonized

79   to act as catalyst during CNT growth; an Al_2O_3 support allows for Fe segregation on the surface

80   to act as the catalyst [27]. The Al_2O_3 support not only influences the active catalyst phase, but it

81   can also have a significant impact on the catalytic activity and lifetime of the particles by

82   mitigating loss of particles through subsurface diffusion and Ostwald ripening [10,12].

83   Various approaches have been taken to overcome limitations to CNT catalyst activity and

84   to improve forest density. For instance, pretreatment of the Fe catalyst using a direct current

85   C_2H_2 plasma was shown to mitigate nanoparticle sintering, affording forest density as high as 0.4

86   g/cm^3 [28]. Among other approaches, a three-layer stack of Al_2O_3-Fe-Al_2O_3 enabled isolation of

87   smaller catalyst particles and gave a higher density forest than the standard two-layer film

88   [29,30], as did a process of cyclic catalyst deposition, annealing, and immobilization by

89   oxidation [31]. With Fe/Al_2O_3 thin films, moisture has also been found to influence the apparent

90   catalyst activity, modulating forest density [32,33]. However, even with a prescribed catalyst

91   and treatment approach, and precise control of the CVD chemistry including moisture,

92   significant run-to-run variations in CNT forest height and density are commonly observed [16].

93   Of these parameters, the role of carbon present before the CNT growth stage is of

94   particular interest. This stems from an observation often made, anecdotally, by frequent growers

95   of CNTs: the consistency and yield of CNT growth using the same quartz furnace tube,

96   repeatedly without cleaning, increase with age of the tube. The walls of an "aged" tube are rich

97   with carbon deposits, which are byproducts from prior growths. Liu *et al*. suggest that such

98   deposits can release hydrocarbon species that assist formation of catalyst particles and improve

99   CNT growth [34]. Also, Chen *et al*. found that adding 4% CH_4 to the H_2 supply during the

100   annealing step helps to form small but high density catalyst particles, and achieve taller forests

101   [35]. A similar effect of high particle density formation was achieved by the C_2H_2 plasma

102   pretreatment utilized by Zhang *et al*., which deposited a 2 nm-thick carbon layer on the substrate

103   before CNT growth [28]. Additionally, Bedewy *et al*. demonstrated *via in situ* ETEM

104   experiments that hydrocarbon exposure was required to fully reduce a Fe film and form

105   nanoparticles suitable for CNT growth, even after prolonged H_2 exposure [17]. Thus, it appears

106   that the time-history of carbon exposure of the catalyst influences the rate and probability of

107   CNT nucleation.

108   Here, we show that atmospheric pressure synthesis of high-density CNT forests is

109   facilitated by controlled exposure of the catalyst to trace carbon species during catalyst

110   nanoparticle formation. We refer to this method as "carbon preloading" and show that it

111   significantly increases CNT forest density and ultimate height, compared to a well-controlled

112   reference process without the trace carbon exposure. We investigate the influence of transient

113   carbon species on the development of the catalyst nanoparticles, and present several hypotheses

114   regarding the underlying mechanisms of this effect of improved CNT forest growth by carbon

115   preload.

2. Experimental

2.1 Sample preparation and CNT synthesis

116

117

118   To prepare substrates for CNT growth, supported catalyst thin films are deposited by

119   sputtering (Lab18, Kurt Lesker) Al_2O_3 (10nm) followed by Fe (1nm) on thermally oxidized

120   (100) silicon wafers. CNT forests are grown at atmospheric pressure using a hot-wall CVD

121   system, comprising a 1" diameter quartz tube within a single-zone furnace (Lindberg Blue Mini-

122   Mite) and electronic mass flow controllers (Aalborg).

123   Two different CVD sequences were used in this study, which we define as the

124   "reference" and "carbon preload" recipes (detailed in **Fig. 1** and the Supplementary Material).

125   The details of the reference recipe have been previously presented in reference [36]: the sample

126   is withdrawn from the hot zone of the furnace (at 775 ^{o}C) after exposure to 400 sccm of H_2 to

127   cause catalyst dewetting, and then it is rapidly reintroduced to the hot zone after the steady

128   mixture of $C_2H_4/H_2/He$ (100/400/100 sccm) is established. However, in the reference process, it

129   is assumed that the Fe dewets completely during exposure to H_2 prior to introduction of C_2H_4. In

130   the carbon preload approach, the tube is conditioned by flowing the mixture of $C_2H_4/H_2/He$

131   (100/400/100 sccm) into the furnace at 775 ^{o}C prior to the dewetting step while the sample

132   remains outside of the furnace hot zone, and the C_2H_4 flow is switched off before the sample is

133   inserted. The sample is therefore annealed for catalyst dewetting in H_2/He only after exposing

134   the furnace (while empty) to a brief duration of C_2H_4 flow, which (as discussed later) appears to

135   deposit a trace amount of carbon on the catalyst, and influence the dewetting and CNT

136   nucleation processes. The influence of the timing and duration of the carbon preload step are

137   discussed later. To ensure consistent conditions from run-to-run (*i.e.* resetting the tube to

138   prevent aging effects), the residual carbon coating the quartz tube is oxidized prior to each run,

139   by heating the tube to 875 ^{o}C with 100 sccm air flow for 30 minutes.

140   The above-mentioned reference and preload recipes at atmospheric pressure yield few-

141   walled CNT forests. Further, synthesis of forests that include single-walled CNTs (SWCNTs) is

142   achieved in a separate hot-wall, low-pressure CVD system, and with the following variations

143   from the recipe as described above: (1) before initiating the recipe, the catalyst substrate is

144   calcinated in air at 400 ^{o}C for 20 min; (2) the atmosphere is maintained at ~400 Torr during

145   annealing and ~100 Torr during growth; and (3) for the growth step, 100 sccm C_2H_4, 800 sccm

146   He, and 200 sccm wet He (100 ppm H_2O) are used to obtain a lower partial pressure of C_2H_4,

147   which is important to SWCNT growth.

148   2.2 *CNT synthesis in ETEM*

149   Transmission electron microscopy (TEM) grids with 10nm thick Si_3N_4 windows were

150   also deposited with 10nm of Al_2O_3 and 1nm of Fe. Experiments were performed in a FEI Titan

151   80-300 ETEM at the Center for Functional Nanomaterials at Brookhaven National Laboratory,

152   using the Si_3N_4 grids. Before each experiment, the ETEM was cleaned for 30 min with O_2

153   plasma and the Gatan single-tilt heating sample holder was plasma cleaned for 10 min. Samples

154   were heated in 40 mTorr H_2 to 650 ^{o}C and annealed for 15 min before introducing 10 mTorr

155   C_2H_2. For a growth study emulating the carbon preload effect, 0.4 mTorr C_2H_2 was also included

156   in the heating and annealing steps. After growth, areas of the sample that were not exposed to

157   the electron beam during growth were checked to confirm there were no significant electron

158   beam effects.

159

160   2.3 *Effluent analysis*

161   For analysis of the gas effluent, a stainless steel canister (Swagelok) was installed in the

162   outlet of the CVD furnace. Gas collection occurred only during the first 5 minutes of the

163   annealing step in each case and then sealed with stainless steel ball valves. Volatile organic

164   compounds (VOCs) were quantified by gas chromatography with a flame ionization detector

165   (GC-FID; SRI 8610C, HayeSep-N, 80/100 mesh, 6'x 1/8" x 0.085", 20 psi He carrier, 50 °C for

166   5 min, 20 °C min^{-1} to 160 °C, 23.5 min hold at 160 °C) calibrated with standard gas mixtures.

167   Gas samples (1 mL) were concentrated using a cryogenic [N_2 (l)] trap of ResSil-C 80/100 mesh

168   silica beads. Unresolved compounds were reported as combined totals of individual standards

169   (*i.e.* propane and propylene, n-butane and 1-butene, n-pentane and 1-pentene). Effluents were

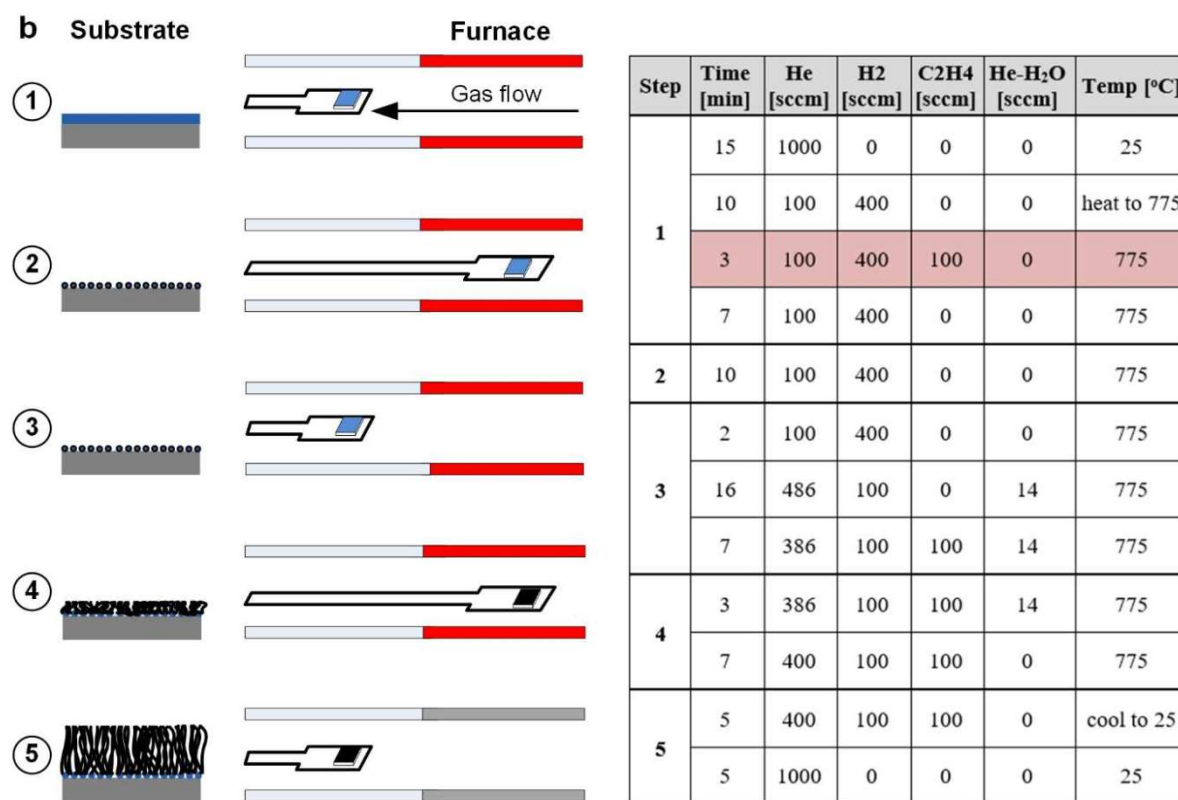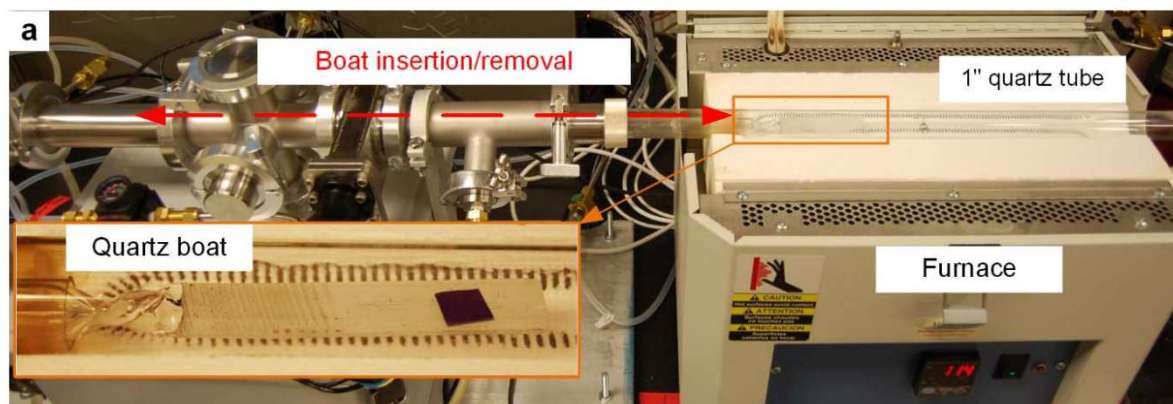170   not measured in the ETEM experiments.

171

172   2.4 *Ex situ characterization*

173   The mass of each CNT forest was obtained by subtracting the post-growth mass (CNTs +

174   substrate) from the substrate mass measured before annealing and growth, using a precision

175   analytical balance (Ohaus Discovery, repeatability of ±0.1 mg). The CNT forest height was

177   were taken using a JEOL 2100 at 200 kV. Raman spectroscopy was performed using a Horiba

178   LabRAM HR800 (532 nm laser). Purity of the forests (weight % CNTs and amorphous carbon)

179   was determined with thermogravimetric analysis using a TA Instruments Discovery TGA at 10

180   $^{\circ}$C/min and the step transition analysis method with TRIOS software. X-ray photoelectron

181   spectroscopy (XPS) analysis was performed using a Kratos Axis Ultra XPS with Al mono

182   source; note that the samples were stored for approximately 1 week in Gel-Pak containers after

183   annealing yet before XPS. Atomic force microscopy (AFM) imaging was performed using a

184   Bruker Dimension Icon in tapping mode and the scan was performed over a 500 x 500 nm square

185   region. Small-angle X-ray scattering (SAXS) characterization was performed at the 12-ID-B

186   beamline at the Argonne National Lab Advanced Photon Source, and the local density at each

187   point in the forest height was obtained using analysis techniques summarized in the

188   Supplementary Material and explained in further detail in reference [37].

Step	Time [min]	He [sccm]	H2 [sccm]	C2H4 [sccm]	He-H2O [sccm]	Temp [ºC]
1	15	1000	0	0	0	25
	10	100	400	0	0	heat to 775
	3	100	400	100	0	775
	7	100	400	0	0	775
2	10	100	400	0	0	775
3	2	100	400	0	0	775
	16	486	100	0	14	775
	7	386	100	100	14	775
4	3	386	100	100	14	775
	7	400	100	100	0	775
5	5	400	100	100	0	cool to 25
	5	1000	0	0	0	25

189
190 **Figure 1. CNT growth procedure with "carbon preload"**. (a) Photo of custom CVD reactor that allows
191 for rapid insertion and removal of a quartz boat (inset) carrying the substrate into the furnace. (b)
192 Schematic sequence of process steps (1-5) for CNT forest synthesis according to the carbon preload
193 recipe, which has sequential gas compositions for each step as noted in the accompanying table; note the
194 carbon preload step is shaded in pink. The transfer arm moves inward from left to right. Red and gray
195 colors on the furnace indicate the furnace is turned on and off, respectively. Further details are in the
196 Supplementary Material.

3. Results and discussion

3.1 *Influence of carbon preload on forest height and density*

First, we assess the height and density of CNT forests (**Fig. 2**), comparing the reference CVD recipe and the carbon preload recipe. The forest height increases approximately linearly with time for the first 10 minutes and is the same for both recipes; however, after 10 minutes the reference recipe stalls (at approximately 1 mm height) but the carbon preload recipe continues and eventually saturates at ~2.3 mm height after 25 minutes. Therefore, from this time series comparison it appears that the carbon preload treatment prolongs the lifetime of the catalyst particle population, allowing the forest to reach a much greater height before self-termination due to density decay.
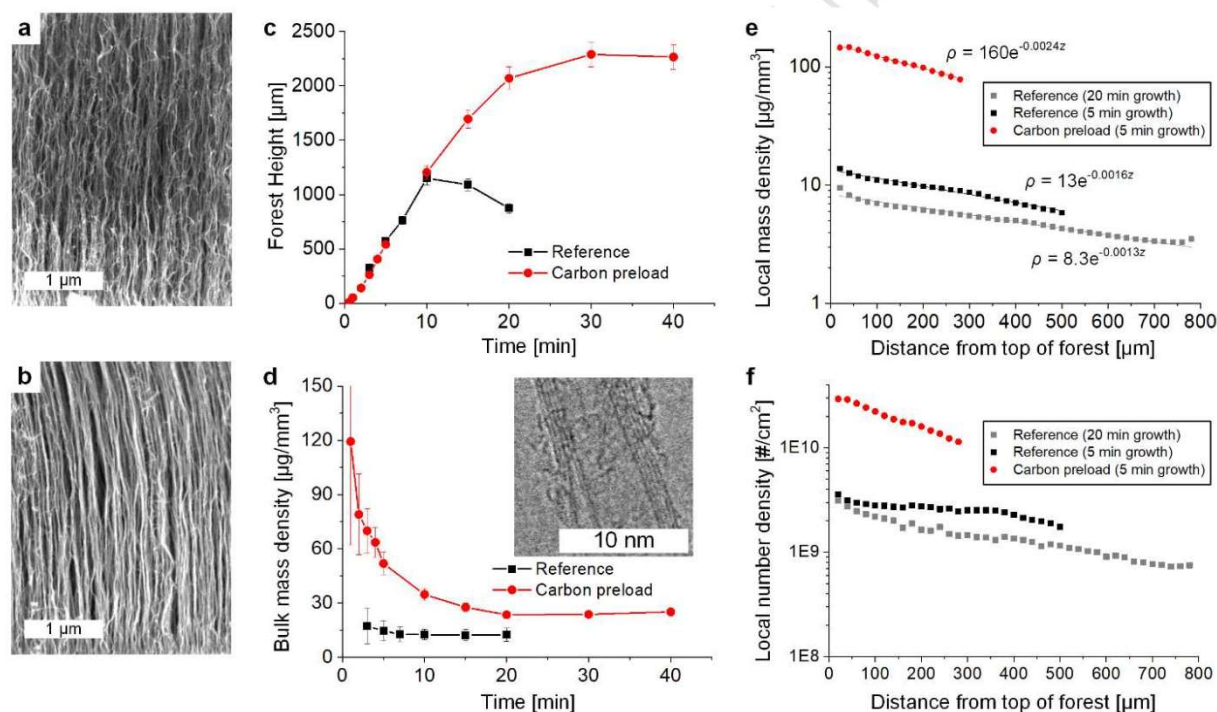
Figure 2. CNT height and density grown by reference and carbon preload recipes. SEM images of the side-wall of a forest grown by (a) reference and (b) preload recipes. (c) Forest heights grown by these two recipes at different growth times. (d) Average forest density, calculated by measured forest height and mass. (e) Local mass and (f) number density obtained by SAXS for forests grown by the reference recipe for 20 minutes (gray) and 5 minutes (black), and by the carbon preload recipe for 5 minutes (red). Exponential fits of mass density ρ vs. position z along the forest height show the nature of local density decay during growth. Note that the peak density was selected as the starting point for the plots, ignoring the measured initial rise in density that might be due to inconsistencies in the height through the thickness of the forest. Because of this and the local nature of the SAXS measurements, the overall forest heights

219   Indeed, CNT forests from both recipes exhibit a density decay with time (*i.e.*, average

220   mass density decreases), yet the carbon preload results in a much greater mass density (**Fig. 2d**).

221   The average density of CNT forests produced by the carbon preload recipe is always greater than

222   that for reference samples grown for the same time, *e.g.* 70 ± 12 μg/mm^3 and 17 ± 10 μg/mm^3 for

223   carbon preload and reference conditions, respectively, for a 3 min growth time. The disparity in

224   density is especially evident for shorter growth times; for instance, the average density of the

225   preload samples is greater than the reference samples by ~4-fold at t = 3 minutes, and ~3-fold at t

226   = 10 minutes (35 ± 3 μg/mm^3 and 13 ± 3 μg/mm^3). Via thermogravimetric analysis (TGA) the

227   forests grown with the carbon preload recipe also have slightly higher purity than the reference

228   recipe: 78% CNT and 20.3% amorphous carbon vs. 74.2% CNT and 22.3% amorphous carbon

229   by weight, respectively (**Fig. S1**). This proves that the measured mass density increase is not due

230   to a byproduct of the carbon preload, and indeed represents an increase in the density of CNTs.

231   Small-angle X-ray scattering was used to profile (at 20 μm increments) the time-varying

232   mass density of the CNT forests [37], comparing samples grown for 5 minutes by each recipe

233   (**Fig 2e**). The top of the forest represents the earliest CNTs, and the base of the forest represents

234   the latest CNTs. This profiling shows that the peak mass density of the forest can be much

235   greater (>10-fold) when using carbon preload, though an exponential decay fit to the data

236   indicates a more rapid density decay for the carbon preload compared to the reference sample

237   (decay rate of 0.0024 vs. 0.0016 μg/mm^3 per μm). Thus, the improvement in mass density of a

238   carbon preload forest prevails up to a limit of exceedingly tall forests.

239   While SAXS measurements suggest a population of slightly larger diameter CNTs for

240   carbon preload forests (**Fig. S2**), the number density of CNTs is also significantly greater with

241   carbon preload; peak densities are 2.9x10^{10} vs. 3.6x10^9 CNTs/cm^2, with vs. without carbon

242   preload, respectively (**Fig. 2f**). This is direct evidence that the carbon preload increases the

243   number of catalyst particles that yield CNTs.

244   A plot of bulk mass density vs. forest height (**Fig. 3**) indicates an inherent trade-off

245   between forest height *h* (*i.e.*, growth time) and achievable mass density ρ, approximated at its

246   upper limit with a power law relationship ($\rho \propto h^{-1/2}$). This data emphasizes that density decay

247   is universal in CNT forest growth, and, comparing our work to reported data from literature, the

248   preload approach gives density values nearly identical to the highest values from prior studies

250   These alternative approaches include pretreatment of the catalyst using a DC plasma containing

251   C_2H_2 [28], utilizing a multi-layer catalyst of thin-Al_2O_3/Fe/thick-Al_2O_3 [29,30], deposition of

252   Al_2O_3 and Fe catalyst from metal complex solutions using dip-coating [38], a controlled slow

253   increase in temperature and precursor supply during growth [39], and precise control of moisture

254   during growth [40–44]. Therefore, the carbon preload approach, which requires no changes to

255   the catalyst materials or substrate preparation, achieves CNT densities that match an apparent

256   maximum observed across the field. This potentially points to a more general (and, previously

257   unexplored) role of trace carbon exposure in mediating catalyst activity for CNT growth, which

258   is addressed in the further experimentation and discussion below.
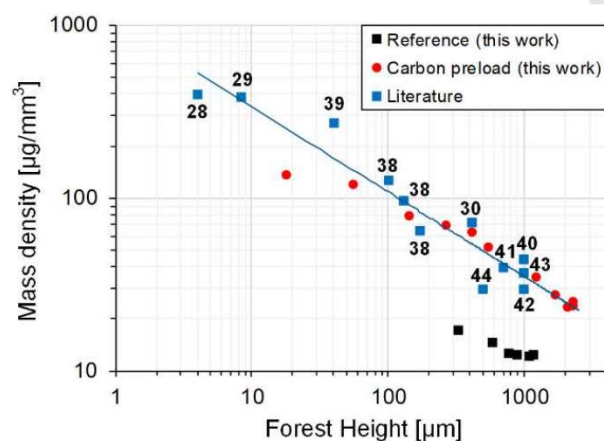
259
260   **Figure 3. Trade-off between forest height and mass density.** CNT forest height vs. mass density from
261   this work and state-of-the-art values reported in literature. The numbers refer to the reference from which
262   the values were obtained. A power law fit to the literature values indicate an upper-bound.
263

264   3.2 *Influence of carbon preload on the catalyst dewetting and particle morphology*

265   In order to assess the influence of the carbon preload on the development of the catalyst,

266   which can certainly influence the viability of the particle population for subsequent CNT

267   nucleation, we characterized substrates that were rapidly withdrawn from the reactor during the

268   annealing stage (*i.e.*, after expected dewetting and particle formation, yet before CNT growth).

269   *Via* AFM image analysis (**Fig. S3**), we find that the preload-treated substrates have a 19%

270   greater number density of catalyst particles than the reference annealed substrates (3.6 x10^{11} per

271   cm^2 and 3.0x10^{11} per cm^2, respectively). Previous work by Chen *et al.* [35] also concluded that

272   annealing of Fe films in a carbon-containing atmosphere (CH_4) resulted in a greater catalyst

273   particle density compared to a control atmosphere high-purity H_2.

274   Raman analysis of the annealed catalyst samples (**Fig. S4**) show no peaks in the range of

275   1100 to 3500 cm^{-1} for the reference sample, but the presence of G, D, and 2D peaks for the

276   preload sample indicates that the carbon preload causes a mixture of sp^2 and sp^3 carbon deposits

277   to form on the catalyst substrate. XPS core scans of Fe 2p (**Fig. S5a**) suggest the presence of

278   iron oxide for both the reference and carbon preload annealed substrates, likely caused by

279   prolonged exposure to atmosphere after completion of the annealing experiments. A core scan

280   of C1s from both substrates (**Fig. S5b,c**) shows there was significant atmospheric contamination,

281   as indicated by the presence of O-C=O peaks ~289 eV and C-O-C peaks ~286 eV. After 20

282   seconds of Ar plasma cleaning, only a weak signal of residual carbon-carbon bond remains on

283   the reference annealed substrate (**Fig. S5d**), whereas the carbon preload annealed substrate (**Fig.**

284   **S5e**) still shows the existence of graphitic carbon from a peak at 285.1 eV with a shoulder

285   towards higher binding energy levels, thereby suggesting carbon incorporation in the catalyst

286   during the preload annealing experiment.

287   To more directly observe the difference between the annealed catalyst particles created

288   under reference and preload conditions (**Fig. 4**), additional control samples after annealing only

289   were processed using Si$_3$N$_4$ TEM grids as the substrates. Subsequent TEM imaging of these

290   substrates showed that the catalyst particles density is greater in the preload case (2.63x10^{11} per

291   cm^2, versus 1.16x10^{11} per cm^2), and the particles are much more clearly defined. This suggests

292   that annealing in a hydrogen-containing atmosphere without added carbon results in a much

293   slower rate of catalyst reduction, and therefore incomplete dewetting. The lower relative density

294   of particles measured by AFM compared to TEM can be attributed to the difficulty of accurate

295   particle counting from images, and substrate effects on the reduction and dewetting methods

296   (Si$_3$N$_4$ vs. SiO$_2$, in spite of the identical alumina underlayer). Nonetheless, the increased particle

297   density under the preload annealing conditions is insufficient to account for the relatively greater

298   increase of initial CNT density (~30-fold), suggesting that the preload treatment also favorably

299   influences the probability of CNT nucleation from the available population of well-formed

300   catalyst nanoparticles. The preload-treated catalysts are coated with graphitic layers, and, in

301   some cases, short CNTs. Additionally, histograms of particle size (**Fig. 4c,f**) taken for TEM

302   images of equal area shows that the particle size distribution on the preload sample is biased

303   toward smaller diameters, indicating that carbon exposure also influences the dewetting
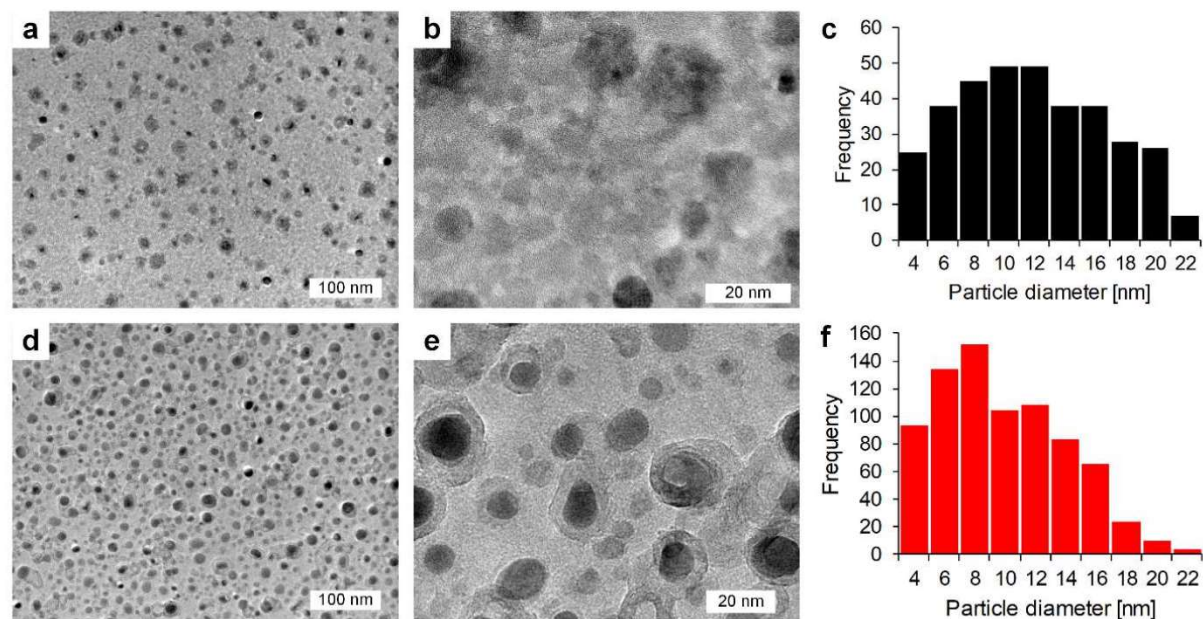
305
306 **Figure 4. Catalyst nanoparticle comparison in TEM.** TEM images of catalyst particles after annealing
307 in a hot-wall CVD reactor with (a,b) reference recipe and (d,e) carbon preload recipe. Graphitic layers
308 and, on some particles, very short CNTs are observed on preload-annealed catalysts. (c,f) Particle density
309 distribution from analysis of images (a) and (d), respectively; each image has area 543 x 543 nm. Note
310 the different scales for frequency in (c) and (f).
311

312   We further substantiate these observations with *in situ* ETEM experimentation. In a prior

313 study using ETEM we found that the formation of nanoparticles from a Fe thin film on Al_2O_3 at

314 low pressure was difficult to induce even with long annealing times in H_2, and full dewetting and

315 reduction of the Fe required exposure to the hydrocarbon precursor (C_2H_2) [17]. Here, ETEM

316 was used to qualitatively observe the influence of trace carbon species on the catalyst, and the

317 possibility to increase CNT density by carbon pre-conditioning. To controllably study this

318 effect, we cleaned the ETEM chamber with 30 minutes of O_2 plasma exposure before performing

319 a reference growth experiment on a catalyst-coated Si_3N_4 TEM grid (650 $^{\circ}$C; 15 min annealing in

320 40 mTorr H_2, adding 10 mTorr of C_2H_2 for CNT growth). Although these conditions resulted in

321 clear dewetting of the catalyst, very few CNTs nucleated upon introduction of the carbon

322 precursor (**Fig. 5a**). By introducing 0.4 mTorr C_2H_2 along with the H_2 during the heating and

323 annealing step (*i.e.* before increasing the C_2H_2 pressure for the CNT growth step), high-density

324 CNT growth was achieved (**Fig. 5b**). While there are important differences between this system

325 and the atmospheric pressure CVD reactor used in the bulk of this study–including the pressure

327 CNTs in the clean ETEM chamber, yet mimicking a carbon-coated chamber gives controllably

328 high-density CNT nucleation.

329
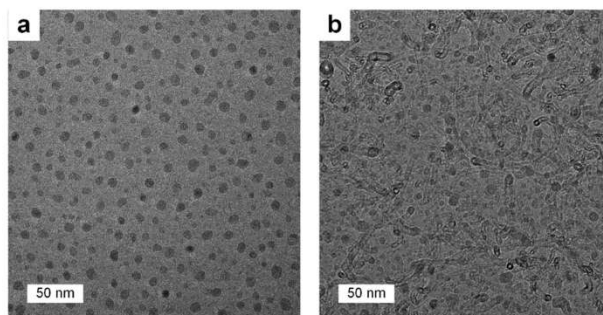
330
331

332 **Figure 5. Preload-assisted CNT growth in environmental TEM**. ETEM images taken after identical
333 CVD growth processes in a clean ETEM chamber at 650 $^{\circ}$C using (a) a reference recipe and (b) a carbon
334 preload technique. The reference condition has few CNTs, while the preload condition has many CNTs
335 along with a higher density of catalyst particles, indicating the need for carbon during
336 dewetting/annealing to achieve high-density CNT growth.

337

338 3.3 *Tracing carbon through the process sequence*

339   The method of carbon preload treatment—exposing the furnace tube to a hydrocarbon

340 flow prior to introduction of the substrate—provides an indirect means to treat the catalyst with a

341 small amount of carbon during the dewetting step of the CNT synthesis process. The duration of

342 tube exposure to the hydrocarbon flow was varied in a series of experiments, and the influence of

343 this duration, which may determine the intensity of carbon exposure communicated *via* the

344 resultant carbon deposits on the reactor, was assessed (**Fig. 6**). Interestingly, we found that

345 exposing the furnace tube to the hydrocarbon for at least 18 seconds was sufficient to result in

346 the significantly greater CNT forest density discussed earlier, yet increasing the tube exposure

347 time to as long as 1800 seconds (30 minutes) resulted in no further CNT density increase. The

348 CNT forest height (here, for 10 minutes CNT growth time) was not changed by the preload

349 duration (or absence thereof), supporting the conclusions of **Figure 2**. Thus, it appears not only

350 that a trace carbon exposure mediated by the tube wall is sufficient to alter the catalyst dewetting

351 and CNT nucleation behavior, but also that the tube wall can be quickly altered into the preload

352 condition. In our system, the lower exposure time limit for an effective carbon preload is likely

353 influenced by the transience in response of the electronic mass flow controllers and resulting
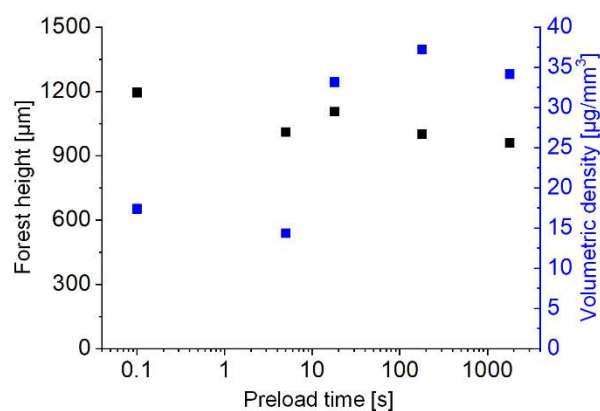
Figure 6. Preload-enhanced CNT forest density is invariant with duration of tube conditioning beyond ~10 seconds, yet CNT forest height is invariant with presence and duration of conditioning.

We now aim to trace the carbon species from its introduction into the tube furnace as C_2H_4 during the preload step to its role in catalyst nanoparticle development. For this, clean quartz substrates were placed in the furnace tube and taken through the preload-annealing sequence, using a 3 minute preload. Afterwards, the samples contained dark deposits as seen with an optical microscope; Raman characterization indicates they are graphitic in nature, according to the presence of the characteristic D and G and G' peaks (**Fig. S6**). Thus, we conclude that the carbon species originating as C_2H_4 is partly transformed into graphitic deposits on the tube, and these deposits form without the presence of the catalyst substrate in the tube.

Next, we sought to determine how the sequence of carbon exposure affected the ability of the carbon to migrate to the catalyst and enhance its activity. We first carbon preloaded just the quartz tube and not the substrate. The preload CVD sequence through the annealing step was performed with an initially clean, empty quartz tube. After cooling, a catalyst substrate was inserted, and the same tube was used to perform a growth with the reference CVD recipe with a catalyst substrate present. In this "modified preload 1" experiment, we found the preload effect of enhanced CNT density is nullified (**Fig. 7**). In other words, the carbon species that enhance catalyst activity do not linger on the tube after cooling, purging, and reheating the tube. A similarly low density is found when the system is pumped and purged between the preload and anneal step of the growth ("modified preload 2"), further confirming the transience of the active carbon species on the tube, and also indicating that these species do not migrate to the substrate

378   and modify the catalyst while it is held outside of the hot zone of the furnace during the

380 into the furnace during the annealing step, carbon species migrate from the tube walls to the

381 catalyst and cause lasting alterations to the catalyst; subsequently cooling down and exposing the

382 catalyst to the atmosphere before resuming the growth ("modified preload 3") still results in a

383 high-density forest.

384
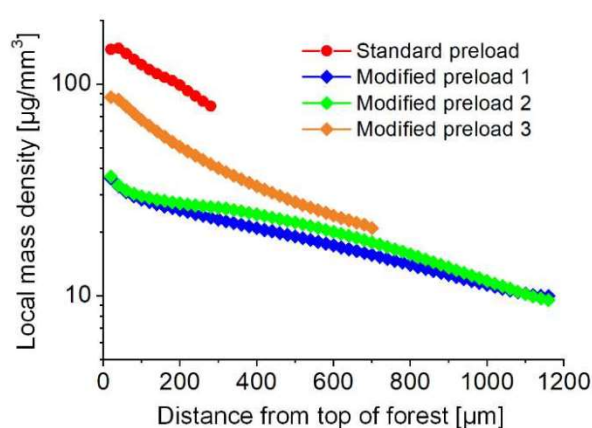
385
386 **Figure 7. Limiting cases of carbon preload conditioning of tube reactor**, showing that the effect of
387 preloading the reactor tube is removed by running the system through a full CVD cycle (modified 1), and
388 that the substrate must be in the hot zone of the furnace to receive the preload effect (modified 2).
389 Annealing the substrate under the preload condition, and then placing the substrate into the reactor for
390 growth after evacuating the tube (modified 3) still resulted in a high CNT density, showing that the
391 carbon exposure during annealing is essential.
392
393 Collection of the reactor effluent (see Experimental section) during the annealing step—

394 both with and without the preload applied—gives insight as to the carbon-containing species that

395 are transferred from the conditioned tube wall to the substrate. **Figure 8** shows the detected

396 amounts of selected short-chain gaseous hydrocarbon species in the effluent. Ethylene is

397 detected in both cases, though in greater amounts for the preload, indicating possible residual

398 ethylene in our CVD system. Backstreaming of the vacuum pump oil may also be a source of

399 the ethylene (from pyrolysis of the oil) and the pentane and pentene, as observed in other CVD

400 studies [45]. Critically, there is a measurable quantity of diverse VOCs, acetylene in particular,

401 in the effluent only for the carbon preload case. Thus, the ethylene supplied during the preload

402 step is forming solids (*e.g.* graphite and soot) or oily compounds (*e.g.* polycyclic aromatic

403 hydrocarbons) that deposit on the tube walls, which subsequently thermally decompose into

404 VOCs under the annealing conditions, when ethylene is no longer being supplied but the catalyst

405 is present inside the furnace. This analysis indicates that carbon preload in the form of ethylene

406   enriches the availability of more active carbon species and possibly activates the catalyst before

407   the dedicated CNT growth step commences.
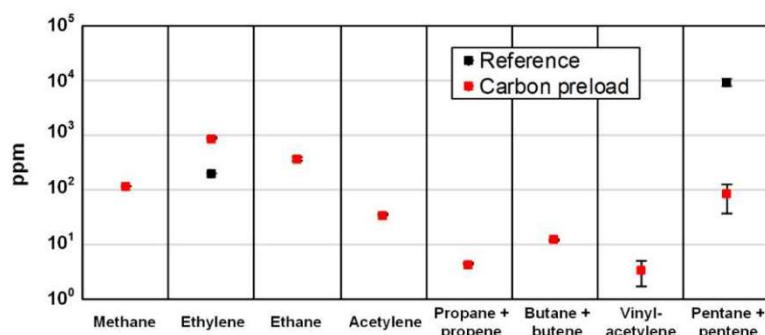
408
409   **Figure 8. Carbon species in the effluent.** Concentration of select carbon species found to be in the
410   effluent from the CVD system during the annealing step, comparing the reference and carbon preload
411   recipes. The absence of data points for many species in the reference condition indicates that the
412   concentration of those species was below the detection limit (~0.5 - 2 ppm, depending on the compound).
413   The compounds reported as combinations were unable to be distinguished and thus the combined values
414   are approximate.

415   3.4 *Carbon preload mechanism*

416   The efficacy of the carbon preload—a means of establishing a well-defined population of

417   active catalyst particles for high-density CNT forest growth—is consistent with prior work which

418   highlights the practical difficulty of reducing iron catalyst films by exposure to H_2 only. *Via*

419   ETEM, we previously observed that the nominally oxidized Fe catalyst film on Al_2O_3 does not

420   fully reduce and dewet. This prevails even upon long exposures to H_2 at high temperatures (750

421    $^{\circ}$C), until a carbon species is introduced, which in turn causes catalyst particles to rapidly form

422   [17]. Additionally, Hofmann *et al.* found *via* XPS that a stronger reducing agent such as NH_3

423   was needed to facilitate complete reduction of Fe [24]; however, using a reducing agent other

424   than pure hydrogen or a hydrocarbon can complicate the catalyst phase dynamics and lead to the

425   creation of non-active catalyst particles (*e.g.* iron nitride when treated with NH_3). Note that these

426   aforementioned ETEM and XPS studies were conducted at low pressure. Other techniques to

427   promote rapid reduction of the catalyst in CVD reactors include using atomic hydrogen

428   (produced by a hot filament) [46,47] and hydrazine vapor [48] as the reducing agent. In

429   addition, *via* systematic studies of alterations to the preload process, we have shown that the

430   carbon species then migrates from the tube walls to the catalyst substrate when it is in the

431   furnace during the annealing step. Characterization of the effluent indicates that the preload

432   process creates reactive carbon species such as C_2H_2 that are known to be more effective

434   Nevertheless, the mechanism by which carbon-loaded catalyst particles result in

435   significantly greater CNT nucleation density requires further investigation. In a companion to

436   the present study, Carpena-Núñez *et al*. [50] showed *via* atmospheric pressure XPS that the CNT

437   nucleation probability increases with the amount of metallic Fe present on the substrate, and that

438   the presence of carbon in the reactor (accumulated due to sequential experimentation) further

439   promotes the reduction of Fe oxide (Fe^{2+}) to metallic Fe (Fe^0).

440   One possible mechanism of enhanced reduction due to the presence of carbon species is

441   carbothermal reduction. Carbon can reduce iron oxide at temperatures above ~700 ^{o}C, as

442   indicated by Ellingham diagrams, and carbothermal reduction is commonly used in metallurgy

443   for producing pure metals [51]. An *in situ* X-ray diffraction study found that, in the absence of

444   H_2 or another reducing agent, C_2H_2 was able to reduce the FeO catalyst at 700 ^{o}C, suggesting

445   carbothermal reduction [52]. The carbon species introduced here by the carbon preload approach

446   might thus be contributing to more efficient reduction of Fe oxide to Fe when we rapidly insert

447   the substrate into the conditioned tube.   Thus, reduction and subsequent dewetting are

448   accelerated, leading to the greater particle availability for CNT nucleation, which we observed

449   *via ex situ* AFM and TEM herein.

450   Moreover, we may expect that reduction and dewetting of the catalyst are further

451   enhanced at higher temperatures, and carbon decomposition on the catalyst can be exothermic

452   [53]. However, as the carbon preload does not significantly blacken the surface of the quartz

453   tube, there is no increase in radiative heating of the substrate. Further, in the ETEM validation

454   experiments only the substrate is heated, decoupling any thermal proximity effects of the reactor

455   wall.   In fact, the ability of the carbon preconditioning to enhance catalyst reduction and

456   dewetting without requiring higher temperatures is advantageous because further heating

457   increases the rate of Ostwald ripening and subsurface diffusion of the catalyst, which can lead to

458   non-uniformity of particle sizes and loss of nucleation sites for CNTs.

459   Notably, the enhancement of the initial CNT population density (*i.e.*, at the top of the

460   forest) is disproportionately greater than the increase in the density of well-formed catalyst

461   particles after annealing. This suggests that carbon exposure increases the probability of CNT

462   nucleation from a Fe catalyst particle, which might be an effect of altered phase dynamics of the

463   catalyst due to the presence of carbon species. Wirth *et al*. suggested that residual carbon

465 from α-Fe; this promotes the predominance of metallic Fe as the catalytically active phase, as

466 opposed to the emergence of Fe_3C as an additional catalytically active phase that forms from

467 predominantly α-Fe nanoparticle distributions [25]. Furthermore, Mazzuco et al. showed that α-

468 Fe can be converted to Fe_3C and nucleate CNTs in the presence of C_2H_2, yet that same Fe_3C can

469 transform into the catalytically inactive Fe_5C_2 phase to terminate CNT growth [26]. Carbon

470 preload might be extending the average lifetime of the catalyst nanoparticles by promoting

471 formation of a metallic Fe phase, which does not allow for this pathway to catalyst deactivation.

472 However, the influence of carbon species on the catalyst phase and the influence of the phase on

473 CNT nucleation efficiency are subjects of further investigation, e.g. with in situ ETEM

474 experimentation that is ongoing.

475   Also, we note that the carbon preload appears to cause graphitic encapsulation of many of

476 the catalyst particles (**Fig. 4**), albeit by ex situ TEM observation of the catalyst after cooling and

477 exposure to ambient. The presence of these graphitic layers suggests that, relative to the particle

478 size, a significant amount of carbon accumulates on and/or within the catalyst due to the preload

479 alone. This might be influencing the initial stage of CNT growth, either by enabling more facile

480 nucleation of a CNT via presence of a solid carbon deposit on the catalyst, and/or by

481 transforming the Fe to a more active phase. The observed graphitic layers that form during the

482 annealing step because of the carbon preload might also be pinning the catalyst nanoparticles,

483 preventing loss of CNT nucleation sites by subsurface diffusion or Ostwald ripening of the

484 catalyst nanoparticles prior to growth.   This is in contrast to the reference case, in which

485 reduction and dewetting are incomplete when the hydrocarbon precursor is introduced, so that

486 there are competing kinetics in the concurrent dynamic processes of particle formation,

487 hydrocarbon dissociation, graphitic species formation, and CNT nucleation and growth. While

488 this work cannot fully isolate or confirm these proposed mechanisms, ongoing work focuses on

489 ETEM observation of catalyst phase dynamics in the presence or absence of transient carbon

490 species during heating and annealing, which will certainly provide further insights.

491   Last, we show that the carbon preload method for enhancing CNT forest growth is

492 applicable to different CVD systems by applying the technique at low pressures to grow forests

493 containing single-wall CNTs. Synthesis of SWCNTs is performed in a separate hot-wall, low-

494 pressure CVD system with slight modifications to the reference and carbon preload recipes (see

496   carbon preload method is 80.2 μm, while that made by the reference method is 26.1 μm.

497   Moreover, Raman spectra (**Figure 9**) show that SWCNTs grown using carbon preload have

498   much higher crystallinity and lower defect level than those grown with the reference recipe;

499   spectra of the middle of the forest sidewall have G/D ratios of 8.6 and 4.5 for carbon preload and

500   reference samples, respectively. The higher yield and crystallinity indicate that the carbon

501   preload method enables more efficient conversion of the supplied carbon source into the

502   graphitic structure of the CNTs. The prominence of radial-breathing mode (RBM) peaks at

503   higher frequencies demonstrates that the preload also reduces the average SWCNT diameter

504   [54]. Thus, carbon preload can improve the growth of both SWCNTs and MWCNTs under

505   different CVD conditions.

506
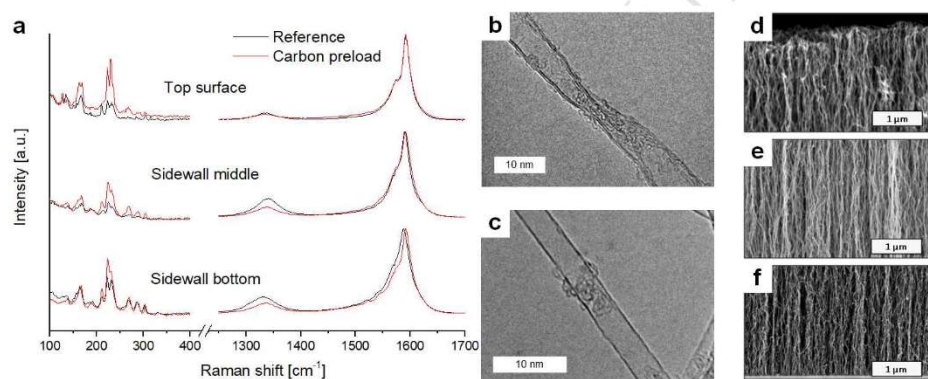
507
508   **Figure 9. Preload-assisted low-pressure growth of SWCNTs.** Growth of a forest containing SWCNTs
509   is achieved in a different CVD system at low pressure. SWCNTs grown by carbon preload are less
510   defective, as indicated by (a) Raman spectra at three different points of each forest, normalized by the G
511   peak height (note the scale is different between the 100-400 cm^{-1} and the 1250-1700 cm^{-1} ranges), and by
512   exemplary TEM images of CNTs grown at low pressure with (b) the reference recipe and (c) carbon
513   preload. SEM images of sidewall of a forest grown at low pressure using carbon preload, at (d) the top,
514   (e) the middle, and (f) the bottom.

515 **4. Conclusion**

516   We have shown that controlled exposure of Fe thin films to trace amounts of carbon

517 during the catalyst dewetting step of a standard CVD process for CNT growth results in

518 significantly enhanced CNT density in the resulting vertically aligned forest. The carbon species

519 were found to adhere to the quartz tube within the furnace and migrate to the catalyst during

520 annealing; these active carbon species (*e.g.* C_2H_2) are transient within the tube, but cause lasting

521 changes (*i.e.* enhanced particle formation and graphitic encapsulation) when exposed to the

522 catalyst. However, the enhanced particle density due to preload does not fully account for the

523 increase in CNT density. We propose that the carbon species aids in reduction of the native Fe

524 oxide catalyst beyond the extent that is possible with just H_2, and this allows for a compound

525 enhancement in CNT nucleation efficiency upon induced hydrocarbon exposure. Further work is

526 necessary to provide mechanistic insight on the catalyst phase dynamics and resulting CNT

527 nucleation efficiency, and to investigate the ability to utilize other forms of carbon for preloading

528 (*e.g.* a solid carbon layer on the catalyst), but the present study realizes a robust experimental

529 approach to repeatably enhance catalyst development for high-density and long lifetime CNT

530 forest growth.

531

ACCEPTED MANUSCRIPT

ACCEPTED MANUSCRIPT

555   **References**

556   [1]   Kaur, S.; Raravikar, N.; Helms, B. A.; Prasher, R.; Ogletree, D. F. Enhanced Thermal
557   Transport at Covalently Functionalized Carbon Nanotube Array Interfaces. *Nat. Commun.*
558   **2014**, *5*, 3082.

559   [2]   Na, N.; Hasegawa, K.; Zhou, X.; Nihei, M.; Noda, S. Denser and Taller Carbon Nanotube
560   Arrays on Cu Foils Useable as Thermal Interface Materials. *Jpn. J. Appl. Phys.* **2015**, *54,*
561   *095102.*

562   [3]   Chiodarelli, N.; Li, Y.; Cott, D. J.; Mertens, S.; Peys, N.; Heyns, M.; *et al.* Integration and
563   Electrical Characterization of Carbon Nanotube *via* Interconnects. *Microelectron. Eng.*
564   **2011**, *88*, 837–843.

565   [4]   Xie, R.; Zhang, C.; van der Veen, M. H.; Arstila, K.; Hantschel, T.; Chen, B.; *et al.*
566   Carbon Nanotube Growth for through Silicon via Application. *Nanotechnology* **2013**, *24*,
567   125603.

568   [5]   Zhou, Y.; Ghaffari, M.; Lin, M.; Parsons, E. M.; Liu, Y.; Wardle, B. L.; *et al.* High
569   Volumetric Electrochemical Performance of Ultra-High Density Aligned Carbon
570   Nanotube Supercapacitors with Controlled Nanomorphology. *Electrochim. Acta* **2013**,
571   *111*, 608–613.

572   [6]   Pint, C. L.; Nicholas, N. W.; Xu, S.; Sun, Z.; Tour, J. M.; Schmidt, H. K.; *et al.* Three
573   Dimensional Solid-State Supercapacitors from Aligned Single-Walled Carbon Nanotube
574   Array Templates. *Carbon* **2011**, *49*, 4890–4897.

575   [7]   Wu, J.; Paudel, K. S.; Strasinger, C.; Hammell, D.; Stinchcomb, A. L.; Hinds, B. J.
576   Programmable Transdermal Drug Delivery of Nicotine Using Carbon Nanotube
577   Membranes. *Proc. Natl. Acad. Sci.* **2010**, *107*, 11698–11702.

578   [8]   Bui, N.; Meshot, E. R.; Kim, S.; Peña, J.; Gibson, P. W.; Wu, K. J.; *et al.* Ultrabreathable
579   and Protective Membranes with Sub-5 Nm Carbon Nanotube Pores. *Adv. Mater.* **2016**, *28*,
580   5871–5877.

581   [9]   Rao, R.; Pint, C. L.; Islam, A. E.; Weatherup, R. S.; Hofmann, S.; Meshot, E. R.; *et al.*
582   Carbon Nanotubes and Related Nanomaterials: Critical Advances and Challenges for
583   Synthesis toward Mainstream Commercial Applications. *ACS Nano* **2018**, *12*, 11756-
584   11784.

585   [10]   Mattevi, C.; Wirth, C. T.; Hofmann, S.; Blume, R.; Cantoro, M.; Ducati, C.; *et al. In-Situ*
586   X-Ray Photoelectron Spectroscopy Study of Catalyst-Support Interactions and Growth of
587   Carbon Nanotube Forests. *J. Phys. Chem. C* **2008**, *112*, 12207–12213.

588   [11]   Kim, S. M.; Pint, C. L.; Amama, P. B.; Zakharov, D. N.; Hauge, R. H.; Maruyama, B.; *et*
589   *al.* Evolution in Catalyst Morphology Leads to Carbon Nanotube Growth Termination. *J.*
590   *Phys. Chem. Lett.* **2010**, *1*, 918–922.

591   [12]   Amama, P. B.; Pint, C. L.; Kim, S. M.; McJilton, L.; Eyink, K. G.; Stach, E. A.; *et al.*
592   Influence of Alumina Type on the Evolution and Activity of Alumina-Supported Fe
593   Catalysts in Single-Walled Carbon Nanotube Carpet Growth. *ACS Nano* **2010**, *4*, 895–
594   904.

595   [13]   Burgos, J. C.; Jones, E.; Balbuena, P. B. Effect of the Metal-Substrate Interaction Strength
596   on the Growth of Single-Walled Carbon Nanotubes. *J. Phys. Chem. C* **2011**, *115*, 7668–
597   7675.

598   [14]   Khalilov, U.; Bogaerts, A.; Neyts, E. C. Atomic Scale Simulation of Carbon Nanotube
599   Nucleation from Hydrocarbon Precursors. *Nat. Commun.* **2015**, *6*, 10306.

601   Model for Self-Assembly of Carbon Nanotubes from Acetylene Based on Real-Time
602   Studies of Vertically Aligned Growth Kinetics. *J. Phys. Chem. C* **2009**, *113*, 15484–
603   15491.

604 [16] Oliver, C. R.; Polsen, E. S.; Meshot, E. R.; Tawfick, S.; Park, S. J.; Bedewy, M.; *et al*.
605   Statistical Analysis of Variation in Laboratory Growth of Carbon Nanotube Forests and
606   Recommendations for Improved Consistency. *ACS Nano* **2013**, *7*, 3565–3580.

607 [17] Bedewy, M.; Viswanath, B.; Meshot, E. R.; Zakharov, D. N.; Stach, E. A.; Hart, A. J.
608   Measurement of the Dewetting, Nucleation, and Deactivation Kinetics of Carbon
609   Nanotube Population Growth by Environmental Transmission Electron Microscopy.
610   *Chem. Mater.* **2016**, *28*, 3804-3813.

611 [18] Meshot, E. R.; Verploegen, E.; Bedewy, M.; Tawfick, S.; Woll, A. R.; Green, K. S.; *et al.*
612   High-Speed *in Situ* X-Ray Scattering of Carbon Nanotube Film Nucleation and Self-
613   Organization. *ACS Nano* **2012**, *6*, 5091–5101.

614 [19] Bedewy, M.; Meshot, E. R.; Reinker, M. J.; Hart, A. J. Population Growth Dynamics of
615   Carbon Nanotubes. *ACS Nano* **2011**, *5*, 8974–8989.

616 [20] Puretzky, A. A.; Geohegan, D. B.; Jesse, S.; Ivanov, I. N.; Eres, G. *In Situ* Measurements
617   and Modeling of Carbon Nanotube Array Growth Kinetics during Chemical Vapor
618   Deposition. *Appl. Phys. A* **2005**, *81*, 223–240.

619 [21] Stadermann, M.; Sherlock, S. P.; In, J.-B.; Fornasiero, F.; Park, H. G.; Artyukhin, A. B.; *et*
620   *al.* Mechanism and Kinetics of Growth Termination in Controlled Chemical Vapor
621   Deposition Growth of Multiwall Carbon Nanotube Arrays. *Nano Lett.* **2009**, *9*, 738–744.

622 [22] Picher, M.; Anglaret, E.; Arenal, R.; Jourdain, V. Self-Deactivation of Single-Walled
623   Carbon Nanotube Growth Studied by *in Situ* Raman Measurements. *Nano Lett.* **2009**, *9*,
624   542–547.

625 [23] Sharma, R.; Moore, E.; Rez, P.; Treacy, M. M. J. Site-Specific Fabrication of Fe Particles
626   for Carbon Nanotube Growth. *Nano Lett.* **2009**, *9*, 689–694.

627 [24] Hofmann, S.; Blume, R.; Wirth, C. T.; Cantoro, M.; Sharma, R.; Ducati, C.; *et al.* State of
628   Transition Metal Catalysts During Carbon Nanotube Growth. *J. Phys. Chem. C* **2009**, *113*,
629   1648–1656.

630 [25] Wirth, C. T.; Bayer, B. C.; Gamalski, A. D.; Esconjauregui, S.; Weatherup, R. S.; Ducati,
631   C.; *et al*. The Phase of Iron Catalyst Nanoparticles during Carbon Nanotube Growth.
632   **2012**, *24*, 4633-4640.

633 [26] Mazzucco, S.; Wang, Y.; Tanase, M.; Picher, M.; Li, K.; Wu, Z.; *et al*. Direct Evidence of
634   Active and Inactive Phases of Fe Catalyst Nanoparticles for Carbon Nanotube Formation.
635   *J. Catal.* **2014**, *319*, 54–60.

636 [27] Oshima, H.; Shimazu, T.; Siry, M.; Ko, M. Analysis of Fe Catalyst during Carbon
637   Nanotube Synthesis by Mossbauer Spectroscopy. *J. Phys. Chem. C* **2009**, *113*, 18523–
638   18526.

639 [28] Zhang, C.; Xie, R.; Chen, B.; Yang, J.; Zhong, G.; Robertson, J. High Density Carbon
640   Nanotube Growth Using a Plasma Pretreated Catalyst. *Carbon* **2013**, *53*, 339–345.

641 [29] Zhong, G.; Warner, J. H.; Fouquet, M.; Robertson, A. W.; Chen, B.; Robertson, J. Growth
642   of Ultrahigh Density Single-Walled Carbon Nanotube Forests by Improved Catalyst
643   Design. *ACS Nano* **2012**, *6*, 2893–2903.

644 [30] Zhong, G. F.; Iwasaki, T.; Kawarada, H. Semi-Quantitative Study on the Fabrication of
645   Densely Packed and Vertically Aligned Single-Walled Carbon Nanotubes. *Carbon* **2006**,

647   [31]   Esconjauregui, S.; Fouquet, M.; Bayer, B. C.; Ducati, C.; Smajda, R.; Hofmann, S.; *et al*.
648   Growth of Ultrahigh Density Vertically Aligned Carbon Nanotube Forests for
649   Interconnects. *ACS Nano* **2010**, *4*, 7431–7436.
650   [32]   Futaba, D. N.; Hata, K.; Yamada, T.; Mizuno, K.; Yumura, M.; Iijima, S. Kinetics of
651   Water-Assisted Single-Walled Carbon Nanotube Synthesis Revealed by a Time-Evolution
652   Analysis. *Phys. Rev. Lett.* **2005**, *95*, 056104.
653   [33]   Shi, W.; Li, J.; Polsen, E. S.; Oliver, C. R.; Zhao, Y.; Meshot, E. R.; *et al*. Oxygen-
654   Promoted Catalyst Sintering Influences Number Density, Alignment, and Wall Number of
655   Vertically Aligned Carbon Nanotubes. *Nanoscale* **2017**, *9*, 5222–5233.
656   [34]   Liu, K.; Liu, P.; Jiang, K.; Fan, S. Effect of Carbon Deposits on the Reactor Wall during
657   the Growth of Multi-Walled Carbon Nanotube Arrays. *Carbon* **2007**, *45*, 2379–2387.
658   [35]   Chen, Z.; Kim, D. Y.; Hasegawa, K.; Noda, S. Methane-Assisted Chemical Vapor
659   Deposition Yielding Millimeter-Tall Single-Wall Carbon Nanotubes of Smaller Diameter.
660   *ACS Nano* **2013**, *7*, 6719–6728.
661   [36]   Li, J.; Bedewy, M.; White, A. O.; Polsen, E. S.; Tawfick, S.; Hart, A. J. Highly Consistent
662   Atmospheric Pressure Synthesis of Carbon Nanotube Forests by Mitigation of Moisture
663   Transients. *J. Phys. Chem. C* **2016**, *120*, 11277–11287.
664   [37]   Dee, N. T.; Bedewy, M.; Rao, A.; Beroz, J.; Lee, B.; Meshot, E. R.; *et al. In Situ*
665   Mechanochemical Modulation of Carbon Nanotube Forest Growth. *Chem. Mater.* **2019**,
666   *31*, 407–418.
667   [38]   Dörfler, S.; Meier, A.; Thieme, S.; Németh, P.; Althues, H.; Kaskel, S. Wet-Chemical
668   Catalyst Deposition for Scalable Synthesis of Vertical Aligned Carbon Nanotubes on
669   Metal Substrates. *Chem. Phys. Lett.* **2011**, *511*, 288–293.
670   [39]   Kawabata, A.; Murakami, T.; Nihei, M.; Yamabe, K.; Yokoyama, N. Evaluation of
671   Thermal Resistance of Carbon Nanotube Film Fabricated Using an Improved Slope
672   Control of Temperature Profile Growth. *Jpn. J. Appl. Phys.* **2015**, *54*, 045101.
673   [40]   Xu, M.; Futaba, D. N.; Yumura, M.; Hata, K. Alignment Control of Carbon Nanotube
674   Forest from Random to Nearly Perfectly Aligned by Utilizing the Crowding Effect. **2012**,
675   *6*, 5837–5844.
676   [41]   Subramaniam, C.; Yamada, T.; Kobashi, K.; Sekiguchi, A.; Futaba, D. N.; Yumura, M.; *et*
677   *al*. One Hundred Fold Increase in Current Carrying Capacity in a Carbon Nanotube-
678   Copper Composite. *Nat. Commun.* **2013**, *4*, 2202.
679   [42]   Futaba, D. N.; Hata, K.; Yamada, T.; Hiraoka, T.; Hayamizu, Y.; Kakudate, Y.; *et al*.
680   Shape-Engineerable and Highly Densely Packed Single-Walled Carbon Nanotubes and
681   Their Application as Super-Capacitor Electrodes. *Nat. Mater.* **2006**, *5*, 987–994.
682   [43]   Futaba, D. N.; Hata, K.; Namai, T.; Yamada, T.; Mizuno, K.; Hayamizu, Y.; *et al*. 84%
683   Catalyst Activity of Water-Assisted Growth of Single Walled Carbon Nanotube Forest
684   Characterization by a Statistical and Macroscopic Approach. *J. Phys. Chem. B* **2006**, *110*,
685   8035–8038.
686   [44]   Matsumoto, N.; Chen, G.; Yumura, M.; Futaba, D. N.; Hata, K. Quantitative Assessment
687   of the Effect of Purity on the Properties of Single Wall Carbon Nanotubes. *Nanoscale*
688   **2015**, *7*, 5126–5133.
689   [45]   Shivayogimath, A.; Mackenzie, D.; Luo, B.; Hansen, O.; Bøggild, P.; Booth, T. J. Probing
690   the Gas-Phase Dynamics of Graphene Chemical Vapour Deposition Using *in-Situ* UV
691   Absorption Spectroscopy. **2017**, 6183.

693   Hydrogen and Active Carbon Species in 1mm Vertically Aligned Single-Walled Carbon
694   Nanotube Growth. *Appl. Phys. Lett.* **2006**, *89*, 123116.

695   [47] Pint, C. L.; Pheasant, S. T.; Pasquali, M.; Coulter, K. E.; Schmidt, H. K.; Hauge, R. H.
696   Synthesis of High Aspect-Ratio Carbon Nanotube "Flying Carpets" from Nanostructured
697   Flake Substrates. *Nano Lett.* **2008**, *8*, 1879–1883.

698   [48] Pint, C. L.; Kim, S. M.; Stach, E. A.; Hauge, R. H. Rapid and Scalable Reduction of
699   Dense Surface-Supported Metal-Oxide Catalyst with Hydrazine Vapor. *ACS Nano* **2009**,
700   *3*, 1897–1905.

701   [49] Plata, D. L.; Meshot, E. R.; Reddy, C. M.; Hart, A. J.; Gschwend, P. M. Multiple Alkynes
702   React with Ethylene to Enhance Carbon Nanotube Synthesis, Suggesting a
703   Polymerization-like Formation Mechanism. *ACS Nano* **2010**, *4*, 7185–7192.

704   [50] Carpena-Núñez, J.; Boscoboinik, J. A.; Saber, S. M.; Rao, R.; Zhong, J.; Maschmann, M.
705   R.; *et al*. Isolating the Roles of Hydrogen Exposure and Trace Carbon Contamination on
706   the Formation of Active Catalyst Populations for Carbon Nanotube Growth. *In review.*

707   [51] Hayward, C. R. Extraction of Metals from Ores. *J. Chem. Educ.* **1943**, *20*, 29–32.

708   [52] Nishimura, K.; Okazaki, N.; Pan, L.; Nakayama, Y. *In Situ* Study of Iron Catalysts for
709   Carbon Nanotube Growth Using X-Ray Diffraction Analysis. *Jpn. J. Appl. Phys.* **2004**,
710   *43*, L471–L474.

711   [53] Harutyunyan, A. R.; Kuznetsov, O. A.; Brooks, C. J.; Mora, E.; Chen, G.
712   Thermodynamics behind Carbon Nanotube Growth *via* Endothermic Catalytic
713   Decomposition Reaction. *ACS Nano* **2009**, *3*, 379–385.

714   [54] Jorio, A.; Saito, R.; Hafner, J. H.; Lieber, C. M.; Hunter, M.; McClure, T.; *et al*. Structural
715   (n, m) Determination of Isolated Single-Wall Carbon Nanotubes by Resonant Raman
716   Scattering. *Phys. Rev. Lett.* **2001**, *86*, 1118–1121.

27